

A new variable shape parameter strategy for RBF approximation using neural networks

Fatemeh Nassajian Mojarrad¹, Maria Han Veiga², Jan S. Hesthaven³, and Philipp Öffner⁴

¹Institute of Mathematics, University of Zürich, Switzerland

²Department of Mathematics, University of Michigan, USA

³Michigan Institute for Data Science, University of Michigan, USA

⁴Chair of Computational Mathematics and Simulation Science, École Polytechnique Fédérale de Lausanne, Switzerland

⁴Institute of Mathematics, Johannes Gutenberg-University Mainz, Germany

Abstract

The choice of the shape parameter highly effects the behaviour of radial basis function (RBF) approximations, as it needs to be selected to balance between ill-condition of the interpolation matrix and high accuracy. In this paper, we demonstrate how to use neural networks to determine the shape parameters in RBFs. In particular, we construct a multilayer perceptron trained using an unsupervised learning strategy, and use it to predict shape parameters for inverse multiquadric and Gaussian kernels. We test the neural network approach in RBF interpolation tasks and in a RBF-finite difference method in one and two-space dimensions, demonstrating promising results.

keywords. Meshfree methods; Radial basis function; Artificial neural network; Variable shape parameter; Unsupervised learning

1 Introduction

Meshfree methods have great advantages over mesh-based methods, since they do not require a grid based domain or surface discretization. The RBF-interpolation is known as a truly meshfree computational method and has the advantage that it is simple to implement and can be applied in complex geometries in high dimensions. Since the values of the RBF depend only on the distance to its center point, RBFs can be easily implemented to reconstruct a hypersurface using scattered data in multi-dimensional spaces [1, 2, 3, 4]. Additionally, for smooth functions, one can reach spectral convergence [5, 6].

Globally supported RBFs often have a shape parameter that plays an important role in the accuracy of the approximation. However, it remains a challenge to find the optimal shape parameter [7, 8, 9, 10]. A small shape parameter results in a poorly conditioned system, but the RBF methods are more accurate. In contrast, a large shape parameter results in well-conditioned matrices, but adversely impacts the accuracy. A depiction of the influence of the choice on the shape parameter ε on the approximation property and condition number of the interpolation matrix is shown in Fig. 1. Thus, the choice of the shape parameter plays an important role and affects both the interpolation error and the stability condition of the RBF.

There exist some attempts to address this problem. For example, one of the early adaptive approaches was proposed by Hardy [11], suggesting $\varepsilon = 1/(0.815d)$, with $d = 1/N \sum_{i=1}^N d_i$, N being the total number of interpolation nodes and d_i being the distance of datapoint i to its nearest neighbour. Another early proposal for adaptive ε was by Franke [12], giving $\varepsilon = \frac{0.8\sqrt{N}}{D}$, where D is the diameter of the smallest circle containing all data points.

Other approaches rely on locally adjusting the shape parameters [9, 13, 7, 10]. Another way to avoid this problem is by evaluating the shape parameter expansion with more advanced algorithms,

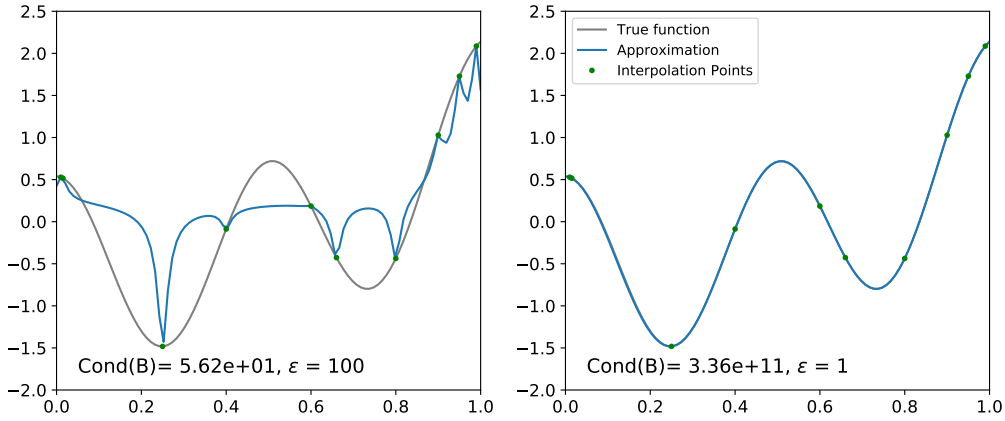


Figure 1: An example of the influence of the choice of ε , and consequently, the condition number of interpolation matrix B , using inverse multiquadratic basis functions (IMQBF).

e.g. allowing complex values or using an efficient rational approximation technique [8, 14]. Even if these ansatzes show promising results, disadvantages remain, e.g. they are not computationally fast nor always very accurate. In this paper we present a new simple approach to select the shape parameter via neural networks (NN), using an unsupervised learning strategy. Our strategy is to learn a map that predicts a shape parameter ε . Once this has been learned, the evaluation of this map is extremely quick, leading to negligible overhead in comparison to a fixed shape parameter.

The outline of the manuscript is as follows: in Section 2, we briefly review the RBF method for interpolation and the local radial basis function based finite difference (RBF-FD) method for both steady-state and time-dependent problems. In Section 3, we introduce some basic concepts of neural networks and demonstrate the use of neural networks to predict the optimal local values of the shape parameter to control the accuracy. In section 4 we test the validity and effectiveness of the proposed strategy, namely, we will test this idea on interpolation problems and solving partial differential equations. Finally, section 5 contains a discussion about the obtained results, as well as future work, and provides some conclusions.

2 Radial Basis Functions (RBF)

RBFs can be used for a variety of tasks. They are good alternatives to interpolate functions on arbitrary sets of multi-dimensional points which, due to the Mairhuber-Curtis theorem, it is not possible with (multivariate) polynomials of degree N to data given at arbitrary locations in \mathbb{R}^n , $n > 1$ [15, 16].

2.1 RBF interpolation

In this section, we introduce the RBF method for the interpolation of scattered data. For a set of N distinct centers $\mathbf{x}_1, \mathbf{x}_2, \dots, \mathbf{x}_N$ in $\Omega \subset \mathbb{R}^d$, the RBF interpolation function can be written in the form

$$S(\mathbf{x}) = \sum_{i=1}^N \lambda_i \phi(\|\mathbf{x} - \mathbf{x}_i\|) + \sum_{k=1}^m \gamma_k \bar{p}_k(\mathbf{x}), \quad (1)$$

where $\|\cdot\|$ denotes the standard Euclidean norm, ϕ is the radial basis function (also called kernel), λ_i represents the unknown interpolation coefficients, γ_k the unknown Lagrange multipliers and $\{\bar{p}_k\}_{k=1}^m$ is a basis for the space of polynomials up to degree $m-1$, denoted by \mathcal{P}_{m-1} . The number of monomial terms is $m = \binom{D_m+2}{2}$, where D_m is the degree of the monomial basis. The RBF interpolant (1) of a

function f is uniquely determined by the conditions

$$\begin{aligned} S(\mathbf{x}_i) &= f(\mathbf{x}_i), \quad i = 1, \dots, N, \\ \sum_{i=1}^N \lambda_i \bar{p}_k(\mathbf{x}_i) &= 0, \quad k = 1, \dots, m. \end{aligned} \quad (2)$$

which are used to calculate the unknown coefficients $\lambda = (\lambda_1, \dots, \lambda_N)^T$ and $\gamma = (\gamma_1, \dots, \gamma_m)^T$. We can reformulate (2) as a linear system to calculate the unknowns. To recover

$$\begin{bmatrix} A & P \\ P^T & 0 \end{bmatrix} \begin{bmatrix} \lambda \\ \gamma \end{bmatrix} = \begin{bmatrix} \mathbf{f} \\ 0 \end{bmatrix}, \quad (3)$$

where $\mathbf{f} = (f(\mathbf{x}_1), \dots, f(\mathbf{x}_N))^T$ and

$$A = \begin{bmatrix} \phi(\|\mathbf{x}_1 - \mathbf{x}_1\|) & \phi(\|\mathbf{x}_1 - \mathbf{x}_2\|) & \dots & \phi(\|\mathbf{x}_1 - \mathbf{x}_N\|) \\ \phi(\|\mathbf{x}_2 - \mathbf{x}_1\|) & \phi(\|\mathbf{x}_2 - \mathbf{x}_2\|) & \dots & \phi(\|\mathbf{x}_2 - \mathbf{x}_N\|) \\ \dots & \dots & \dots & \dots \\ \phi(\|\mathbf{x}_N - \mathbf{x}_1\|) & \phi(\|\mathbf{x}_N - \mathbf{x}_2\|) & \dots & \phi(\|\mathbf{x}_N - \mathbf{x}_N\|) \end{bmatrix}, P = \begin{bmatrix} \bar{p}_1(\mathbf{x}_1) & \dots & \bar{p}_m(\mathbf{x}_1) \\ \bar{p}_1(\mathbf{x}_2) & \dots & \bar{p}_m(\mathbf{x}_2) \\ \dots & \dots & \dots \\ \bar{p}_1(\mathbf{x}_N) & \dots & \bar{p}_m(\mathbf{x}_N) \end{bmatrix}. \quad (4)$$

We denote by $B = \begin{bmatrix} A & P \\ P^T & 0 \end{bmatrix}$ and assume that the solution in any point $\mathbf{y} \in \Omega$ can be written in the form

$$\begin{aligned} S(\mathbf{y}) &= \underbrace{(\phi(\|\mathbf{y} - \mathbf{x}_1\|), \dots, \phi(\|\mathbf{y} - \mathbf{x}_N\|), \bar{p}_1(\mathbf{y}), \dots, \bar{p}_m(\mathbf{y}))}_{q(\mathbf{y})} \begin{bmatrix} \lambda \\ \gamma \end{bmatrix} \\ &= (q(\mathbf{y})B^{-1})_{1:N} \mathbf{f} = \sum_{i=1}^N f(\mathbf{x}_i) [q(\mathbf{y})B^{-1}]_i = \sum_{i=1}^N f(\mathbf{x}_i) \Psi_i(\mathbf{y}), \end{aligned} \quad (5)$$

where Ψ_i are called cardinal functions. They build a basis of the underlying approximation space. Commonly used types of radial basis functions are listed in Table 1. In this work, we use the inverse multiquadratic RBF

$$\phi(r) = \frac{1}{\sqrt{1 + (\varepsilon r)^2}},$$

and the Gaussian RBF with the shape parameter $\varepsilon > 0$. The condition number of matrix B depends on the shape parameter ε as illustrated in Fig. 1.

Table 1: Common RBF types.

Type of basis function	$\phi(r)$
Gaussian	$e^{-(\varepsilon r)^2}$
Multiquadric	$\sqrt{1 + (\varepsilon r)^2}$
Inverse quadratic	$\frac{1}{1 + (\varepsilon r)^2}$
Inverse multiquadric	$\frac{1}{\sqrt{1 + (\varepsilon r)^2}}$
Polyharmonic spline	$r^k, k = 1, 3, 5, \dots$ $r^k \ln(r), k = 2, 4, 6, \dots$

Remark 2.1. Inclusion of polynomials up to a certain degree inside the RBF interpolation (1) has several advantages:

- The RBF interpolants becomes exact for polynomials up to a certain degree. Including constants is necessary for the RBF method to be conservative [17, 18].
- For some (unconditionally) positive kernels ϕ , the RBF interpolant exists uniquely when polynomials up to a certain degree are included [1].
- It has a positive influence on the accuracy of the RBF-FD method [6].

In our work, we will also include constants in our RBF (1) interpolant.

2.2 RBF-FD method for solving steady-state and time dependent differential equations

The RBF-FD method is a meshfree method to solve partial differential equations (PDEs) numerically, which arose from the global RBF methods [2]. Solving PDEs with global RBF methods results in remarkable numerical aspects like time stability and accuracy. However, the high computational cost and memory requirements of RBF for very large problem sizes is the main reason for the development of RBF-FD method [2]. RBF-FD formulas are generated from RBF interpolation over local sets of nodes on the surface [19], i.e.: only a nearest neighbour region is connected to each basis function. This means that we have a clustering of point clouds where the cardinal basis are considered locally inside the cloud. This leads to a sparse matrix instead of the full linear system of equations. Next, we derive the RBF-FD formulation [20] for Poisson and time dependent differential equations.

We are interested in the solution of the Poisson equation

$$\Delta u(\mathbf{x}) = f(\mathbf{x}) \quad \text{or} \quad \mathcal{L}u(\mathbf{x}, t) = f(\mathbf{x}), \quad \mathbf{x} \in \Omega, \quad (6)$$

where Δ is the Laplace operator and \mathcal{L} denotes the space differential operator which can be also used in a more general setting. Equation (6) is complemented by boundary conditions. The domain Ω is discretized using two point sets:

- The interpolation point set $X = \{\mathbf{x}_i\}_{i=1}^N$ for generating the cardinal functions.
- The evaluation point set $Y = \{\mathbf{y}_j\}_{j=1}^M$ for sampling the PDE (6).

The cardinality of X and Y point sets matches the relation $M = rN$, where r is the oversampling parameter. We use collocation and oversampled discretization, where in the collocation discretization we set $Y = X$.

Using (5), we evaluate the numerical solution at the evaluation point $\mathbf{y} \in Y$ as follows

$$\begin{aligned} u(\mathbf{y}) &= \underbrace{(\phi(\|\mathbf{y} - \mathbf{x}_1\|), \dots, \phi(\|\mathbf{y} - \mathbf{x}_N\|), \bar{p}_1(\mathbf{y}), \dots, \bar{p}_m(\mathbf{y}))}_{q(\mathbf{y}, X)} \begin{bmatrix} \lambda \\ \gamma \end{bmatrix} \\ &= (q(\mathbf{y}, X)B(X, X)^{-1})_{1:N} u(X) = \sum_{i=1}^N u(\mathbf{x}_i) [q(\mathbf{y}, X)B(X, X)^{-1}]_i = \sum_{i=1}^N u(\mathbf{x}_i) \Psi_i(\mathbf{y}), \end{aligned} \quad (7)$$

where $\Psi_i(\mathbf{y})$, $i = 1, \dots, N$ are again the cardinal basis functions developed at the interpolation X . We represent the domain using the nodal points X . Then, we assume n nearest neighbour points for each \mathbf{x}_i , denoted $\mathcal{N}(\mathbf{x}_i)$ [21]. These neighbours are called node's support domain or stencil. We form a local interpolation problem by using (7) on each stencil point set $\mathcal{N}(\mathbf{x}_i)$. We can write the approximation of $u(\mathbf{y})$ in stencil set $\mathcal{N}(\mathbf{x}_i)$ as: for $i = 1, \dots, N$

$$u^{(i)}(\mathbf{y}) = \sum_{k=1}^n u(\mathbf{x}_k^{(i)}) [q(\mathbf{y}, \mathcal{N}(\mathbf{x}_i))B(\mathcal{N}(\mathbf{x}_i), \mathcal{N}(\mathbf{x}_i))^{-1}]_k = \sum_{k=1}^N u(\mathbf{x}_k^{(i)}) \psi_k^{(i)}(\mathbf{y}), \quad (8)$$

where $\psi_k^{(i)}(\mathbf{y})$ are the local cardinal functions. To obtain a global solution at \mathbf{y} , we associate every evaluation point with an index of the closest stencil center point defined by

$$\nu(\mathbf{y}) = \arg \min_{i \in \{1, \dots, N\}} \|\mathbf{y} - \mathbf{x}_i\|$$

This means that $\mathbf{y} \in \mathcal{N}(\mathbf{x}_{\nu(\mathbf{y})})$, and we have

$$u(\mathbf{y}) = u^{(\nu(\mathbf{y}))}(\mathbf{y}) = \sum_{k=1}^N u(\mathbf{x}_k^{(\nu(\mathbf{y}))}) \psi_k^{(\nu(\mathbf{y}))}(\mathbf{y}), \quad (9)$$

and analogously for f in (6). It follows in a similar fashion that

$$\mathcal{L}u(\mathbf{y}) = \mathcal{L}u^{(\nu(\mathbf{y}))}(\mathbf{y}) = \sum_{k=1}^N u(\mathbf{x}_k^{(\nu(\mathbf{y}))}) \mathcal{L}\psi_k^{(\nu(\mathbf{y}))}(\mathbf{y}), \quad (10)$$

which is used in the discretization.

Let us consider the linear boundary value problem

$$\frac{\partial u(\mathbf{x}, t)}{\partial t} = \mathcal{L}u(\mathbf{x}, t), \quad \mathbf{x} \in \Omega, \quad 0 \leq t \leq T, \quad (11)$$

$$u(\mathbf{x}, t) = g(\mathbf{x}, t), \quad \mathbf{x} \in \partial\Omega, \quad (12)$$

$$u(\mathbf{x}, 0) = f(\mathbf{x}), \quad \mathbf{x} \in \Omega. \quad (13)$$

where $\Omega \subset \mathbb{R}^d$ is the solution domain with the boundary $\partial\Omega$ where Dirichlet boundary conditions are considered and \mathcal{L} is a differential operator on \mathbb{R} .

By using a simple method of lines (MOL) approach, we split between space and time discretization. For the space discretization our local RRB-FD discretization is applied and the time integration uses classical schemes like Runge-Kutta (RK) methods, backward differentiation formulas (BDFs) or deferred correction schemes (DeC). The only difference lies in the discretization of (10) where the coefficients are now depending as well on time, i.e.

$$\mathcal{L}u(\mathbf{y}, t) = \mathcal{L}u^{(\nu(\mathbf{y}))}(\mathbf{y}, t) = \sum_{k=1}^N u(\mathbf{x}_k^{(\nu(\mathbf{y}))}, t) \mathcal{L}\psi_k^{(\nu(\mathbf{y}))}(\mathbf{y}) \quad (14)$$

and we obtain a linear system of ordinary equations from (11) to involve the time dependent coefficients $u(\mathbf{x}_k^{(\nu(\mathbf{y}))}, t)$.

In this work we consider (6) or (11) with Dirichlet boundary conditions. We impose the boundary conditions in two ways: (a) when studying the eigenvalue spectra, we remove the values of the vector $u(\mathbf{x}, t)$ located on the boundary, along with the corresponding columns and rows in the matrices, (b) when computing the numerical solution in time, we use the injection method to impose the condition, i.e., we overwrite the solution $u(\mathbf{x}, t_i), i = 0, 1, \dots$ with the corresponding boundary value, after each step of the time-stepping algorithm. Note that these two procedures are equivalent.

3 Methodology

As mentioned before, the most accurate results are obtained for shape parameter which yields an ill-conditioned system matrix. Therefore, we can formulate our goal as follows:

We want to find a function f for which given a set of n arbitrary points, denoted as a vector $\vec{x} \in \mathbb{R}^n$, returns ε such that the condition number of the interpolation matrix $M(\vec{x}, \varepsilon)$, generated using radial basis functions, \vec{x} and ε , is close to some large value cond_{\max} at the *edge of* being ill-conditioned:

$$f : \vec{x} \in \mathbb{R}^n \rightarrow \varepsilon \quad \text{s.t.} \quad \text{cond}(M(\vec{x}, \varepsilon)) \approx \text{cond}_{\max}. \quad (15)$$

3.1 Dataset generation

We consider m sets of n arbitrary points in the interval $[0, 1]$. These define our interpolation nodes, which we will refer to as *coordinate-based features*.

We can also generate a different set of features, called *distance-based features*. From the interpolation points, we define $n - 1$ distances as:

$$\begin{aligned} d_1 &= x_2 - x_1 \\ &\dots \\ d_{n-1} &= x_n - x_{n-1} \end{aligned}$$

Note that $x_j - x_i = \sum_{l=i}^{j-1} d_l$ and thus can write the interpolation matrix (4) in terms of the distance vector (d_1, \dots, d_{n-1}) .

For the 1-dimensional problem, it is advantageous to use distance-based features as the dimension is reduced and we have a shift-invariance property. We also observe experimentally that the distance-based features appear to lead to a better performance across different problems.

First, we consider the inverse of the distances. Then we center and normalise all data points i :

$$x_i^j = \frac{x_i^j - \bar{x}^j}{\sigma^{j^2}}, \quad j = 1, \dots, d$$

for d denoting the number of features, \bar{x} the empirical mean and σ^{j^2} the empirical variance across all training points.

For construction of a training sample, we consider samples of n uniformly distributed points over $[0, 1]$. The training and validation datasets are constructed using the distances between these points. We consider a total of 4400 training samples and 1100 validation samples.

3.2 Data driven model

We consider a dense, fully connected neural network (DFC NN) to approximate the map in (15). We assume that f is approximated by \mathcal{H} of the form:

$$\mathcal{H}(\vec{x}) := \sigma_p(\dots \sigma_1(A_1 \vec{x} + b_1)), \quad (16)$$

for activation functions σ_i , and trainable parameters $\mathbf{W} = \{A_i, b_i\}$, for $i = 1, \dots, p$. A_i is a matrix in $\mathbb{R}^{d_i \times d_{i-1}}$ and b_i is vector in \mathbb{R}^{d_i} , d_0 is the input dimension (n for coordinate-based features and $n - 1$ for distance-based features), and d_p is the output dimension ($d_p = 1$).

The structure of the neural network for $n = 10$ and distance-based features has the following parameters: $p = 4$, $d_0 = 9$, $d_1 = 14$, $d_2 = 8$, $d_3 = 3$, $d_4 = 1$, with ReLU activation function for $p = 1, 2, 3$ and linear activation for $p = 4$.

We train the neural network with respect to the following cost function, for a data point \vec{x}_j :

$$C_j(\mathbf{W}) = \begin{cases} 0.1 \times \log(-\text{cond}(B_j) + 10^{10} + \kappa), & \text{if } \text{cond}(B_j) \leq 10^{10}, \\ 0, & \text{if } 10^{10} < \text{cond}(B_j) \leq 10^{12}, \\ \log\left(\frac{10}{9}(\text{cond}(B_j) - 10^{12}) + \kappa\right), & \text{if } 10^{12} < \text{cond}(B_j) \leq 10^{13}, \\ \log(\text{cond}(B_j) + \kappa), & \text{if } \text{cond}(B_j) > 10^{13}, \end{cases} \quad (17)$$

where $\kappa = 1$ and $\text{cond}(B_j) = \|B_j\|_F \|B_j^{-1}\|_F$, B_j is the interpolation matrix built using the interpolation nodes \vec{x}_j and the predicted ε . The loss function is as in (17) to ensure that it is continuous, and to enforce that the condition number B_j is between 10^{10} and 10^{12} .

Since we work with condition numbers and we use a gradient descent based method to compute the model parameters, we consider a logarithmic cost function to have a smaller magnitude update in the weights at each iteration of the optimisation algorithm.

Furthermore, special care must be taken to ensure that the trained network does not overfit the training dataset. A common method to avoid overfitting is to regularize the cost functional by penalizing the parameters \mathbf{W} of the network [22]

$$\mathcal{R}(\mathbf{W}) = \beta \|\mathbf{W}\|_2^2, \quad (18)$$

where $\beta \geq 0$ is the regularization parameter and $\|\mathbf{W}\|_2^2$ represents the squared sum of all the weights in the MLP.

Thus, the cost function across a given minibatch of size S_b is

$$C(\mathbf{W}) = \frac{1}{S_b} \sum_{j=1}^{S_b} C_j(\mathbf{W}) + \beta \|\mathbf{W}\|_2^2,$$

where we take $S_b = 500$.

Remark 3.1. We emphasize that this learning task does not fall into the standard supervised learning framework. We do not have access to an optimal ε for each set of nodes \vec{x} . The network is optimised with respect to the defined loss function by finding a suitable ε that leads to a matrix with a desired matrix condition number. We set this condition number to be close to 10^{12} .

In addition, we have an early stopping criteria [22]. We use a validation data set which is independent of the training set. Once the loss computed on the validation data set stagnates after M consecutive epochs, the training is terminated and we recover the best set of parameters. Fig. 2 shows the plots of training loss and validation loss.

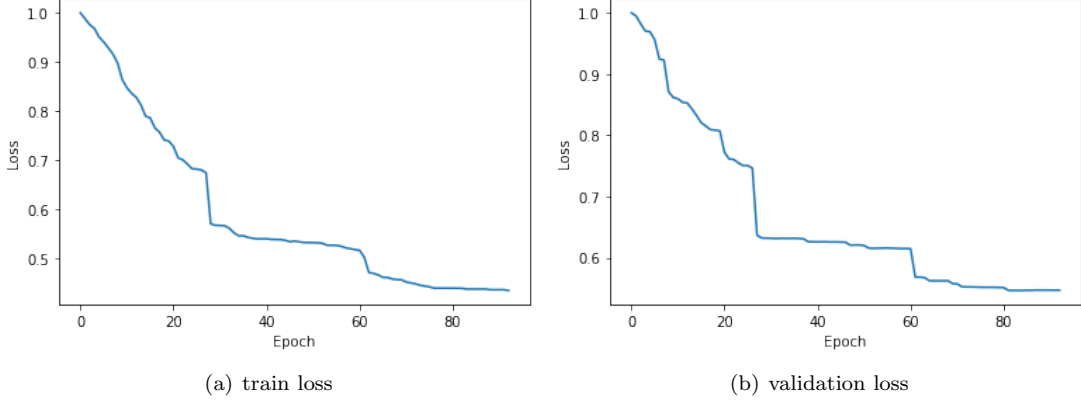


Figure 2: Loss during training in 1D with IMQRBf.

3.3 Extension to 2-dimensional problems

We also consider an extension of this method to 2-dimensional problems. For the dataset generation and representation, we have again two options: *coordinate-based features* and *distance-based features*.

In a 2-dimensional problem, the advantage of considering coordinate-based features is clearer, because the number of features per number of interpolation nodes scales as $2 \times n$, whereas for distances, we have $\binom{n}{2}$ features. However, when adopting a coordinate-based feature representation we lose the shift-invariant property.

In our work, we extend the proposed methodology to a non-generic distribution of 2-dimensional points. In particular, we consider only structured distributions of points (as shown in Fig. 3, for $n = 9$). This constraint on the distribution of points allows the simplification of the description of the cloud of points when considering distance-based features.

The 2-dimensional feature vector for the coordinate-based representation yields:

$$x_{2D} = ((x_i - x_{mid})_{1 \leq i \leq n}, (y_i - y_{mid})_{1 \leq i \leq n}), \quad (19)$$

where $x_{mid} = \frac{1}{n} \sum_{i=1}^n x_i$ and $y_{mid} = \frac{1}{n} \sum_{i=1}^n y_i$.

The distance-based features yields:

$$x_{2D} = (\Delta y, 2\Delta y, \Delta x, \sqrt{\Delta x^2 + \Delta y^2}, \sqrt{\Delta x^2 + (2\Delta y)^2}, 2\Delta x, \sqrt{(2\Delta x)^2 + \Delta y^2}, 2\sqrt{\Delta x^2 + \Delta y^2}). \quad (20)$$

Using the same procedure as described for the 1D case, we consider the inverse of the distances, center and normalise all data points.

The structure of the neural network for $n = 9$ and distance-based features in two dimensions has the following parameters: $p = 4$, $d_0 = 8$, $d_1 = 16$, $d_2 = 8$, $d_3 = 3$, $d_4 = 1$, with ReLU activation function for $p = 1, 2, 3$ and linear activation for $p = 4$. In 2D, we consider a few test cases and when the condition number of interpolation matrix is near 10^{12} , we terminate training of the neural network.

4 Numerical results

In this section, several problems are considered to demonstrate the accuracy of using distance-based features in one and two dimensions. We also present the results obtained with coordinate-based features in one dimension in Appendix A. The MLP is trained with an initial learning rate of $\eta = 10^{-4}$ and the

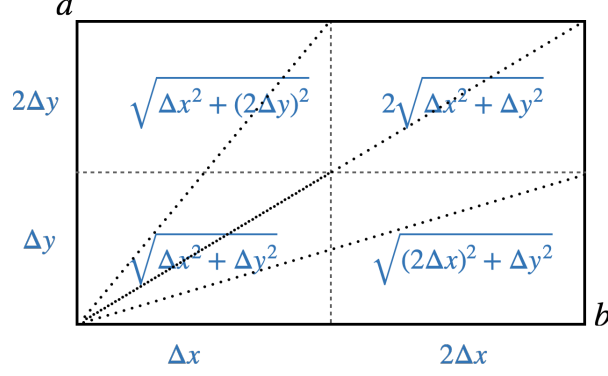


Figure 3: Structured distribution for 9 nodes. The parameters $a, b \in [0, 1]$ define the shape of the rectangle, $\Delta x = b/2$, $\Delta y = a/2$.

regularization parameter is set to $\beta = 10^{-5}$. In the computations, the oversampling parameter r is set to 4.

The errors reported are using the L_1 -error between the approximation and exact solutions:

$$L_1\text{-error} = \frac{1}{N} \sum_{i=1}^N |u_e(\mathbf{x}_i) - u_a(\mathbf{x}_i)|$$

where u_e and u_a are the exact and approximate solutions, respectively.

4.1 Numerical results for 1D test cases

Following the method in section 3.2, we train a neural network to predict the shape parameter ε . We consider two different kernels: the inverse multiquadratic radial basis functions (IMQRBF) and the Gaussian radial basis function (GARBF). We also vary the number of points considered to build the interpolation as $n = 5, 7, 10$.

Fig. 4 demonstrates the performance of the trained neural network, using distance-based features, for $n = 10$ stencil with IMQRBF and GARBF kernels. In the left panel, we show the average condition number of the interpolation matrix obtained as the distance between the nodal points diminishes (this occurs as we increase the number of points N considered in the interval $[0, 1]$). In the right panel, we show the predicted shape parameter again as the distance between nodal points decreases. In particular, we see that the predicted ε increases as the distances decrease, as expected. Furthermore, we observe a similar behaviour when we consider $n = 5$ and 7.

In the next two sections, we will test this neural network on two specific tasks: interpolation (section 4.1.1) and for solving a time-dependent problem (4.1.2).

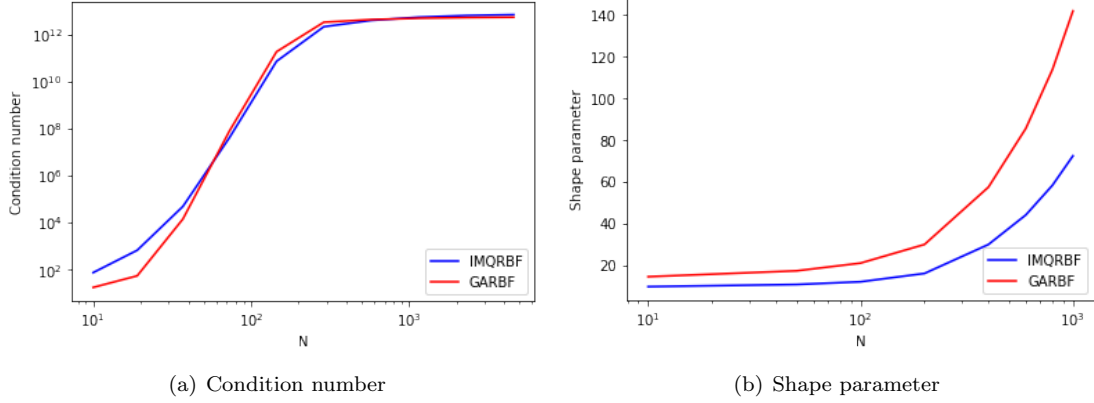


Figure 4: Condition number and shape parameter for different values of N for IMQRBf and GARBf.

4.1.1 Interpolation

Two functions are used to examine the numerical accuracy of the present variable shape parameter strategy in the one-dimensional interpolation. We compare the proposed method with the constant shape parameter, Hardy [23], Franke [24] and modified Franke strategies. For all the interpolation task, the domain is discretized with the equidistant and non-equidistant centers and the refined mesh is obtained by adding the midpoints in each step. We then consider sets of n points to construct the interpolation, overlapping the boundary node between clusters.

The function f_1 is an exponential and trigonometric combination:

$$f_1(x) = e^{\sin(\pi x)} \quad x \in [0, 1].$$

We first consider the IMQRBf kernel. Fig. 5 shows the convergence plot for varying neural network input sizes for the function f_1 for equidistant points. Therefore, we can observe that an appropriate choice of the points is $n = 10$.

Fig. 6 shows the convergence plot for the function f_1 using shape parameters obtained by the neural network strategy and the constant shape parameters $\varepsilon = 10, 100, 1000$ as a function of the number of centers for equidistant and non-equidistant points. Note that as N increases, when using fixed ε , we run into the issue that the matrix becomes too ill-conditioned and we are unable to produce a suitable interpolation function, this is why, for example, for $\varepsilon = 10$, we can only reach $N \approx 10^4$.

Fig. 7 compares the convergence when using shape parameters obtained by the neural network and the adaptive methods Hardy, Franke and modified Franke strategies, as a function of the number of centers for equidistant and non-equidistant points. While these approaches always produce interpolation functions for this problem, the RBFs with shape parameters obtained by neural network provides interpolation functions with a much better to interpolate function f_1 .

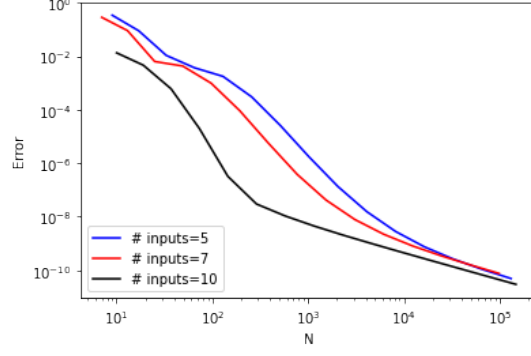


Figure 5: Convergence plot for the function f_1 using different input sizes for a neural network with IMQRBf.

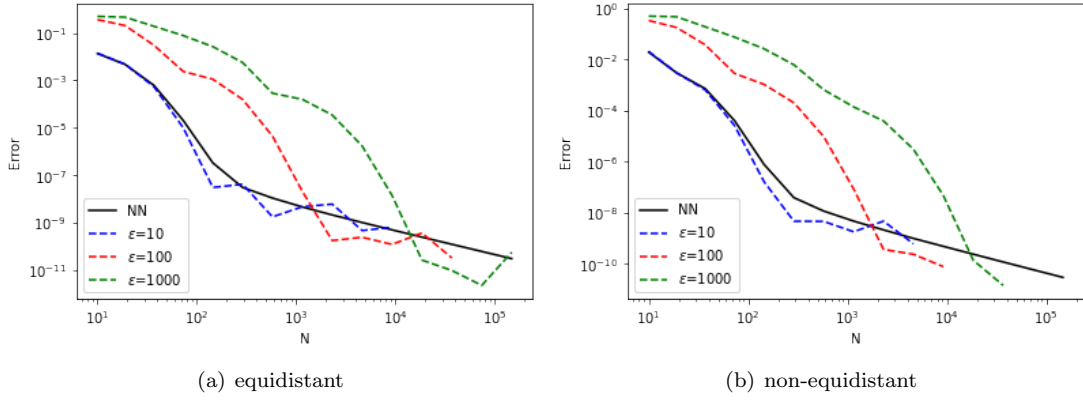


Figure 6: Convergence plot for the function f_1 using a neural network strategy and constant shape parameters in 1D with IMQRBf.

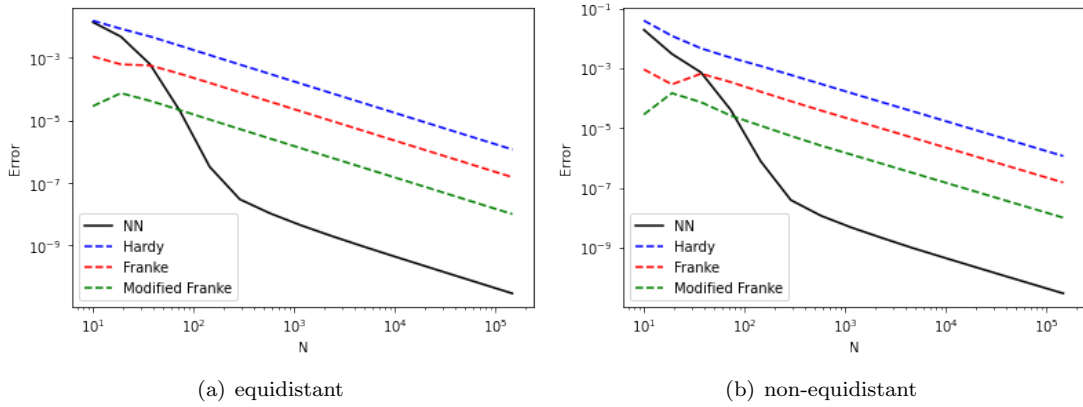


Figure 7: Convergence plot for the function f_1 using a neural network, Hardy [23], Franke [24] and modified Franke strategies in 1D with IMQRBf.

We now consider function f_2 , the well known Runge function, a rational function:

$$f_2(x) = \frac{1}{1 + 16x^2}, \quad x \in [0, 1].$$

Again, we focus first on the IMQRBF kernel. In Fig. 8 we show the convergence plot for varying neural network input sizes for the function f_2 for equidistant points. The results look very similar to those shown in 5, and thus, we present the results using the $n = 10$ neural network.

In Fig. 9, we show the convergence plot using shape parameters obtained by the neural network strategy and constant shape parameters ($\varepsilon = 10, 100, 1000$) as a function of the number of centers for equidistant and non-equidistant points. Again, we note that as N increases, at some point the fixed ε will fail as 6 produces interpolation matrices which are too ill-conditioned and we are unable to produce a suitable interpolation function.

Fig. 10 shows the convergence plot using shape parameters obtained by the neural network, Hardy, Franke and modified Franke strategies as a function of the number of centers for equidistant and non-equidistant points. Again, we observe much smaller error when using the neural network.

We plot also the resulting interpolation function for $N = 19$ and $N = 37$, comparing the variable and constant shape parameter strategies in Fig. 11. We obtain similar results using the GARBF kernel for both interpolation tasks, which can be found in Appendix B.1.

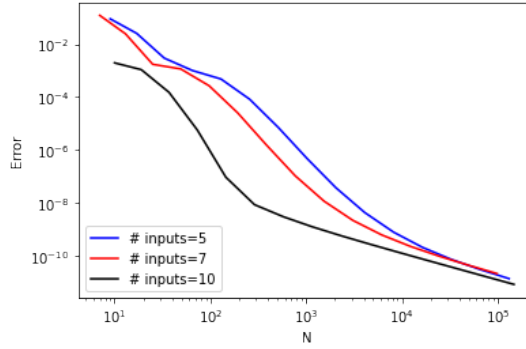


Figure 8: Convergence plot for the function f_2 using different input sizes for a neural network with IMQRBF.

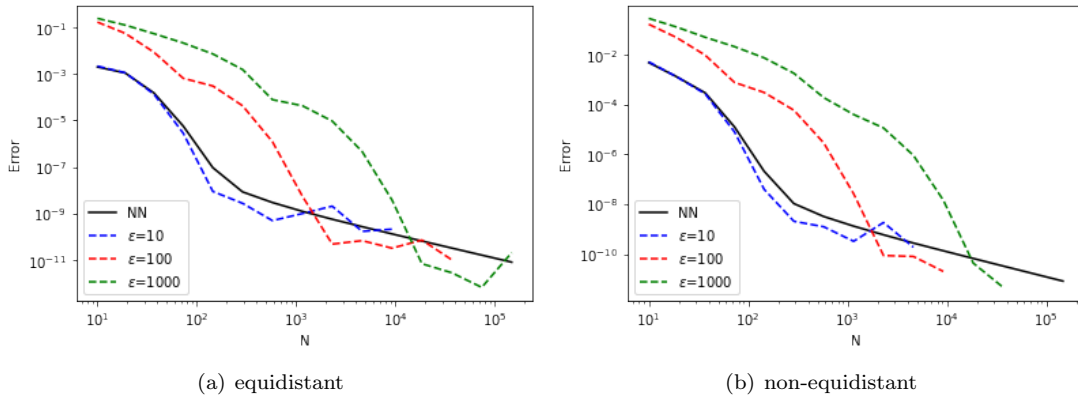


Figure 9: Convergence plot for the function f_2 using a neural network strategy and constant shape parameters in 1D with IMQRBF.

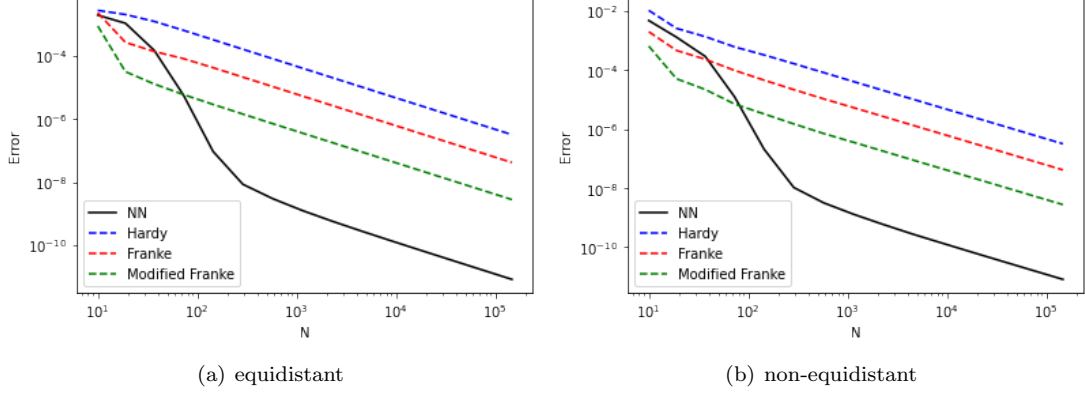


Figure 10: Convergence plot for the function f_2 using a neural network, Hardy, Franke and modified Franke strategies in 1D with IMQRBF.

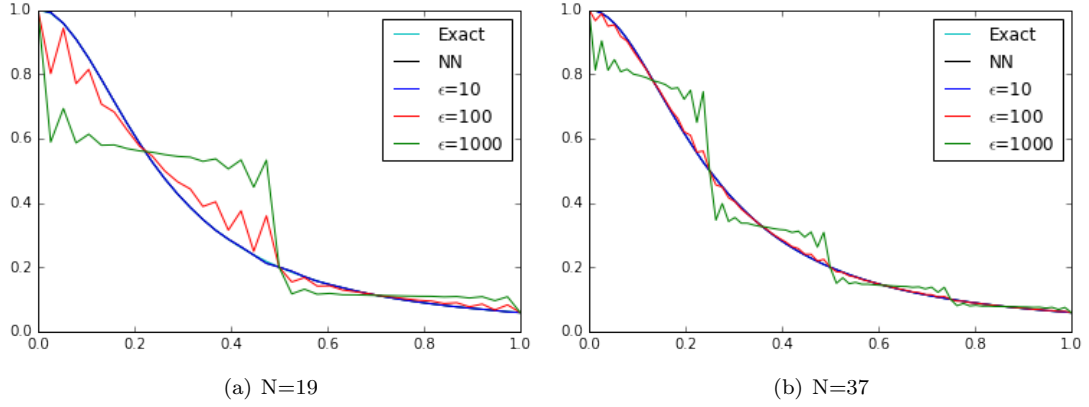


Figure 11: Comparison between variable and constant shape parameter strategies for f_2 for $N = 19$ and $N = 37$ with IMQRBF.

4.1.2 Time-dependent problem

We have tested the NN strategy on a heat equation with two different initial conditions, and compare the RBF-FD method with the shape parameters obtained by the neural network strategy with finite difference method (FDM), finite element method (FEM) and RBF-FD method with constant shape parameters. We use BDF2 for time stepping in all cases. We use the same technique as in the previous section to obtain the refined mesh.

The first test case is the heat equation governed by

$$\frac{\partial u}{\partial t} = \frac{\partial^2 u}{\partial x^2}, \quad x \in [0, 1], \quad 0 \leq t \leq 1, \quad (21)$$

with the initial condition

$$u(x, 0) = -x^2 + x, \quad x \in (0, 1), \quad (22)$$

and the boundary conditions

$$u(0, t) = 0, \quad u(1, t) = 0, \quad 0 \leq t \leq 1. \quad (23)$$

The exact solution of (21) with initial condition (22) and boundary conditions (23) is given by

$$u(x, t) = \sum_{n=1}^{\infty} \left(\frac{-4}{n^3 \pi^3} \right) ((-1)^n - 1) \sin(n\pi x) e^{-n^2 \pi^2 t}.$$

We set $\Delta t = 0.001$. The errors are shown in Table 2 and Table 3 for equidistant and non-equidistant points, obtained with IMQRBF kernel. Firstly, we show that for our method, the error decreases consistently under mesh refinement for the equidistant points while it remains bounded for the non-equidistant points, attaining comparable performances to the FDM, FEM methods and RBF method with a fixed shape parameter $\varepsilon = 10$. For the fixed shape parameter $\varepsilon = 1$, we are unable to attain a suitable numerical solution beyond $N = 19$, and for $\varepsilon = 100$, we observe a generally approximation error. We obtain similar results using a Gaussian kernel, shown in Appendix B.

Table 2: The error using different schemes for equidistant points with initial condition $-x^2 + x$ with IMQRBF.

N	FDM	FEM	NN	$\varepsilon = 1$	$\varepsilon = 10$	$\varepsilon = 100$
N=10	1.5283e-04	1.5152e-04	5.4703e-03	6.9435e-06	5.9731e-03	1.4708e-02
N=19	4.1141e-05	3.9723e-05	5.8909e-04	8.6638e-07	6.0268e-04	1.5342e-02
N=37	1.1152e-05	9.8825e-06	5.0922e-05	-	4.4987e-05	1.4919e-02
N=73	3.3997e-06	2.4375e-06	4.4037e-06	-	2.9077e-06	1.0560e-02
N=145	1.4322e-06	9.6827e-07	1.3377e-06	-	9.0652e-07	1.1204e-03

Table 3: The error using different schemes for non-equidistant points with initial condition $-x^2 + x$ with IMQRBF.

N	FDM	FEM	NN	$\varepsilon = 1$	$\varepsilon = 10$	$\varepsilon = 100$
N=10	3.0018e-03	3.1917e-03	9.2538e-03	2.9977e-03	9.5229e-03	1.4744e-02
N=19	3.1257e-03	3.1769e-03	4.0141e-03	3.1253e-03	4.0648e-03	1.5521e-02
N=37	3.2019e-03	3.2151e-03	3.7890e-03	-	3.7745e-03	1.5813e-02
N=73	3.2435e-03	3.2469e-03	3.3382e-03	-	3.2918e-03	1.4598e-02
N=145	3.2653e-03	3.2662e-03	3.2660e-03	-	3.2652e-03	8.4020e-03

As a second test, we consider again the heat equation (21) now with the different initial condition

$$u(x, 0) = 6 \sin(\pi x), \quad x \in (0, 1) \quad (24)$$

and the boundary conditions

$$u(0, t) = 0, \quad u(1, t) = 0, \quad 0 \leq t \leq 1. \quad (25)$$

The exact solution is given by

$$u(x, t) = 6 \sin(\pi x) e^{-\pi^2 t}.$$

In Table 4 and Table 5 the error are listed for equidistant and non-equidistant points with IMQRBF, respectively. The differences between RBF- FD with shape parameters obtained by neural network and RBF-FD with constant shape parameter are not significant. Neural network has similar performance to $\varepsilon = 10$ but a superior performance when compared to $\varepsilon = 1$ and $\varepsilon = 100$. Also, the differences between RBF- FD with shape parameters obtained by the neural network, FDM and FEM are not significant for non-equidistant points. Moreover, we can see that the results of the new strategy, FDM and FEM are approximately the same for equidistant points as long as N is not too low.

We obtain similar results when considering the GARBF kernel, which can be found in Appendix B.2.

Table 4: The error using different schemes for equidistant points with initial condition $6 \sin(\pi x)$ with IMQRBF.

N	FDM	FEM	NN	$\varepsilon = 1$	$\varepsilon = 10$	$\varepsilon = 100$
N=10	3.5303e-03	3.4600e-03	1.2696e-01	6.2511e-05	1.3867e-01	3.4160e-01
N=19	9.4294e-04	9.1108e-04	1.3518e-02	1.7241e-05	1.3833e-02	3.5640e-01
N=37	2.5361e-04	2.2566e-04	1.1860e-03	-	1.0468e-03	3.4678e-01
N=73	7.5759e-05	5.4121e-05	1.0088e-04	-	6.5944e-05	2.4553e-01
N=145	3.0626e-05	2.0276e-05	2.8705e-05	-	1.8624e-05	2.6311e-02

Table 5: The error using different schemes for non-equidistant points with initial condition $6 \sin(\pi x)$ with IMQRBf.

N	FDM	FEM	NN	$\varepsilon = 1$	$\varepsilon = 10$	$\varepsilon = 100$
N=10	6.9932e-02	7.4578e-02	2.1597e-01	6.9815e-02	2.2221e-01	3.4248e-01
N=19	7.2790e-02	7.4039e-02	9.3362e-02	7.2770e-02	9.4567e-02	3.6052e-01
N=37	7.4552e-02	7.4875e-02	8.8268e-02	-	8.7929e-02	3.6743e-01
N=73	7.5520e-02	7.5602e-02	7.7758e-02	-	7.6662e-02	3.4017e-01
N=145	7.6028e-02	7.6048e-02	7.6045e-02	-	7.6025e-02	1.9665e-01

4.2 Numerical results for 2D test cases

We generate the interpolation and evaluation point sets in two dimensions using regular Cartesian meshes. For the structured grid, again, similarly to the results in one dimension, we note that the condition number remains well controlled for varying distances of points, and that the shape parameter increases as the distances between points decreases, as expected. We show the condition number and shape parameter values for different values of N and M using the IMQRBf kernel in Fig. 12. We observe a similar behaviour when considering the GARBF kernel.

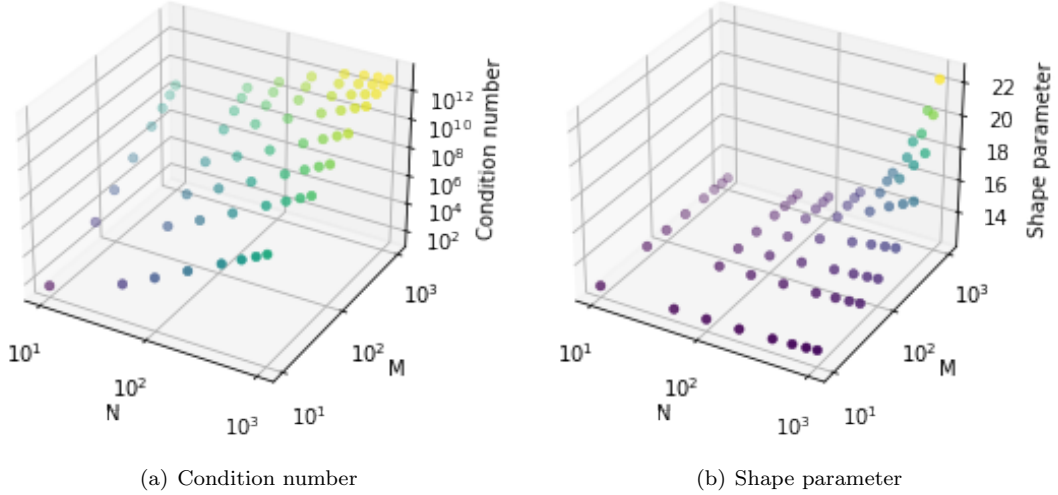


Figure 12: Condition number and shape parameter for different values of N and M for IMQRBf.

4.2.1 Interpolation

Our numerical experiment of the present strategy, involves interpolating two functions in two dimensions. We approximate Franke's function [1]

$$f_3(x, y) = \frac{3}{4}e^{-\left(\frac{(9x-2)^2 + (9y-2)^2}{4}\right)} + \frac{3}{4}e^{-\left(\frac{(9x+1)^2}{49} + \frac{(9y+1)^2}{10}\right)} \\ + \frac{1}{2}e^{-\left(\frac{(9x-7)^2 + (9y-3)^2}{4}\right)} - \frac{1}{5}e^{-\left((9x-4)^2 + (9y-7)^2\right)}$$

where $(x, y) \in [0, 1] \times [0, 1]$. The proposed NN method has been compared with a constant shape parameter strategy ($\varepsilon = 1, 5, 10, 100$).

We perform a convergence study for RBF-FD method using the GARBF kernel and we compare the results using the neural network and constant shape parameter strategies ($\varepsilon = 1, 5, 10, 100$). The results are shown in table 6. We note that when using this kernel, there is a greater sensitivity to the choice of ε and thus, we see a clear advantage to having an adaptive strategy when picking ε .

Table 6: The error using RBF-FD method using different strategies for interpolating f_3 for structured grid with GARBF.

# interpolation points	# evaluation points	NN	$\varepsilon = 1$	$\varepsilon = 5$	$\varepsilon = 10$	$\varepsilon = 100$
10×10	20×20	4.0537e-03	4.0578e-03	3.9408e-03	7.4077e-03	3.2520e-02
20×20	40×40	3.7430e-03	4.4900e-04	5.5438e-04	2.3120e-03	1.2673e-02
40×40	80×80	5.4949e-04	6.8680e-05	6.7709e-05	3.0185e-04	5.1903e-03
80×80	160×160	7.0266e-05	7.9787e-03	8.2785e-06	3.7286e-05	9.3109e-04
160×160	320×320	9.2307e-06	1.6475e-01	4.8958e-06	4.6122e-06	4.4077e-04
320×320	640×640	1.3128e-06	1.5472e-01	1.2479e-03	4.8370e-06	6.1821e-05

When considering the RBF-FD method using the IMQRBF kernel, we observe a similar error decay for NN and $\varepsilon = 10$, as shown in Table 7. Furthermore, we plot the numerical solution obtained by using NN and constant shape parameters with 640×640 evaluation points is given in Fig. 13. We only report the results with $\varepsilon = 1, 5, 10$, since the results for $\varepsilon = 100$ is of similar nature.

Table 7: The error using RBF-FD method using different strategies for interpolating f_3 for structured grid with IMQRBF.

# interpolation points	# evaluation points	NN	$\varepsilon = 1$	$\varepsilon = 5$	$\varepsilon = 10$	$\varepsilon = 100$
10×10	20×20	4.3784e-03	3.7428e-03	3.3664e-03	4.5244e-03	2.3411e-02
20×20	40×40	2.3193e-03	4.2816e-04	6.3583e-04	1.8377e-03	5.5466e-03
40×40	80×80	5.1059e-04	5.0617e-05	8.6087e-05	3.3993e-04	3.5434e-04
80×80	160×160	7.6687e-05	1.0758e-03	1.0795e-05	4.6778e-05	7.2623e-04
160×160	320×320	1.0667e-05	3.6852e-02	1.4960e-06	5.9460e-06	3.0940e-04
320×320	640×640	1.5576e-06	7.3941e-02	1.7185e-04	9.8128e-07	6.3065e-05

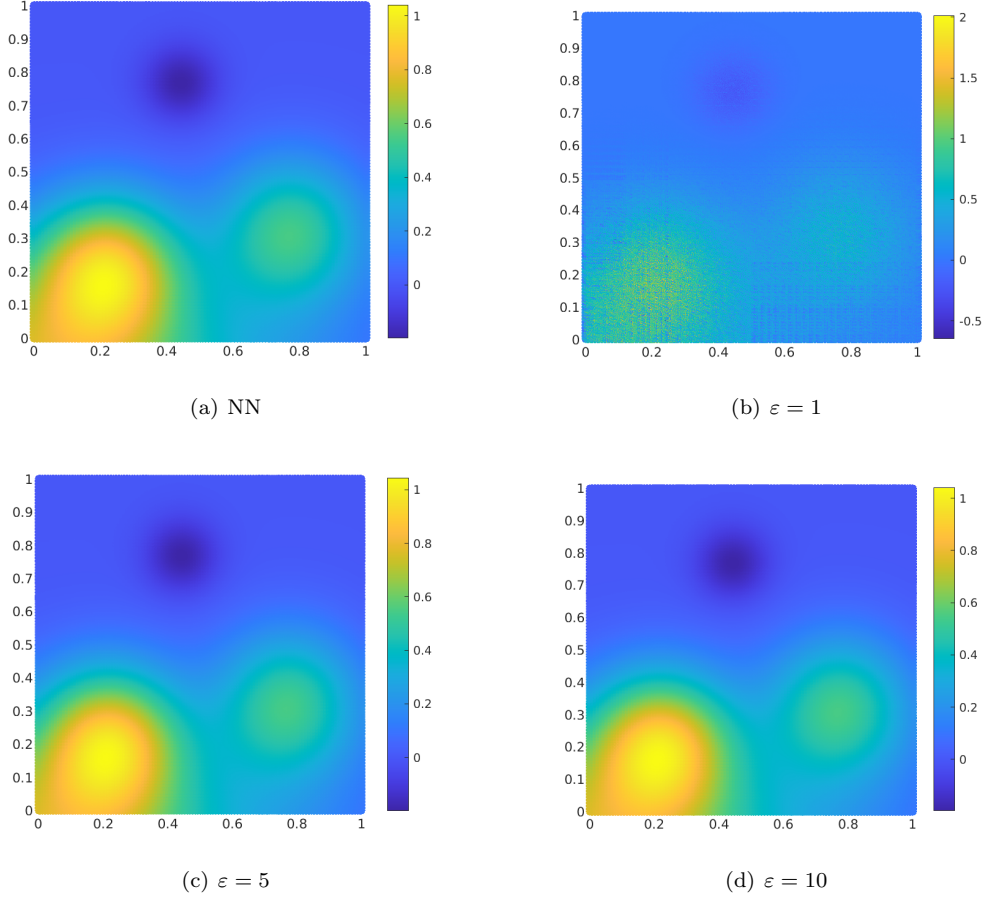


Figure 13: Numerical solution for the function f_3 using 640×640 evaluation points with IMQRBF.

The next test function is taken from [25, 26, 27]. We consider the function

$$f_4(x, y) = (1 + e^{-\frac{1}{\alpha}} - e^{-\frac{x}{\alpha}} - e^{\frac{(x-1)}{\alpha}})(1 + e^{-\frac{1}{\alpha}} - e^{-\frac{y}{\alpha}} - e^{\frac{(y-1)}{\alpha}}), \quad (x, y) \in [0, 1] \times [0, 1].$$

As $\alpha > 0$ decreases, the problem becomes more difficult. In Table 8 we present the corresponding results using GARBF kernel for the same numbers of interpolation and evaluation points, whereas in Table 9 we present the corresponding results using IMQRBFs. In terms of errors, they are very similar to the results for the previous test case. The numerical solution obtained by using the neural network and constant shape parameters with 640×640 evaluation points for $\alpha = 0.1$ is shown in Fig. 14.

Table 8: The error using RBF-FD method using different strategies for interpolating f_4 for structured grid with GARBF.

	# interpolation points	# evaluation points	NN	$\varepsilon = 1$	$\varepsilon = 5$	$\varepsilon = 10$	$\varepsilon = 100$
$\alpha = 1$	10×10	20×20	1.9268e-04	1.5882e-05	2.8331e-04	4.6367e-04	1.4925e-03
	20×20	40×40	1.8951e-04	1.7094e-06	3.4351e-05	1.2386e-04	6.4021e-04
	40×40	80×80	2.7365e-05	1.5040e-06	4.0265e-06	1.5767e-05	2.4397e-04
	80×80	160×160	3.4516e-06	3.3276e-04	4.8374e-07	1.9183e-06	4.4864e-05
	160×160	320×320	4.4844e-07	7.0042e-03	1.9386e-07	2.3545e-07	2.0077e-05
	320×320	640×640	6.4760e-08	6.5279e-03	5.1445e-05	2.0242e-07	2.8334e-06
$\alpha = 0.1$	10×10	20×20	2.6965e-02	1.1568e-02	2.6705e-02	3.7388e-02	9.7074e-02
	20×20	40×40	1.2069e-02	1.4181e-03	3.3277e-03	8.4496e-03	3.8001e-02
	40×40	80×80	1.7349e-03	1.9894e-04	3.8974e-04	1.0688e-03	1.3912e-02
	80×80	160×160	2.1546e-04	1.9756e-02	4.6063e-05	1.2804e-04	2.5090e-03
	160×160	320×320	2.7536e-05	4.1583e-01	1.3108e-05	1.5523e-05	1.1248e-03
	320×320	640×640	3.9773e-06	3.8633e-01	3.0628e-03	1.2252e-05	1.5898e-04

Table 9: The error using RBF-FD method using different strategies for interpolating f_4 for structured grid with IMQRBF.

	# interpolation points	# evaluation points	NN	$\varepsilon = 1$	$\varepsilon = 5$	$\varepsilon = 10$	$\varepsilon = 100$
$\alpha = 1$	10×10	20×20	2.5032e-04	3.1038e-05	2.2328e-04	2.8326e-04	1.0485e-03
	20×20	40×40	1.1963e-04	3.3140e-06	3.8237e-05	9.7860e-05	2.7322e-04
	40×40	80×80	2.5064e-05	4.4151e-07	4.9931e-06	1.7203e-05	1.7237e-05
	80×80	160×160	3.7100e-06	4.0940e-05	6.1578e-07	2.3282e-06	3.3546e-05
	160×160	320×320	5.1081e-07	1.5014e-03	7.8305e-08	2.9357e-07	1.4084e-05
	320×320	640×640	7.3937e-08	2.7727e-03	7.2542e-06	4.7251e-08	2.8793e-06
$\alpha = 0.1$	10×10	20×20	2.7700e-02	1.2855e-02	2.3944e-02	2.8308e-02	7.3125e-02
	20×20	40×40	8.1087e-03	1.5699e-03	3.5878e-03	6.9354e-03	1.8655e-02
	40×40	80×80	1.5816e-03	1.8545e-04	4.4749e-04	1.1406e-03	1.6996e-03
	80×80	160×160	2.2833e-04	2.4572e-03	5.3792e-05	1.5055e-04	1.8506e-03
	160×160	320×320	3.0922e-05	8.9455e-02	6.7846e-06	1.8757e-05	7.8172e-04
	320×320	640×640	4.4105e-06	1.6994e-01	4.3497e-04	3.0998e-06	1.6067e-04

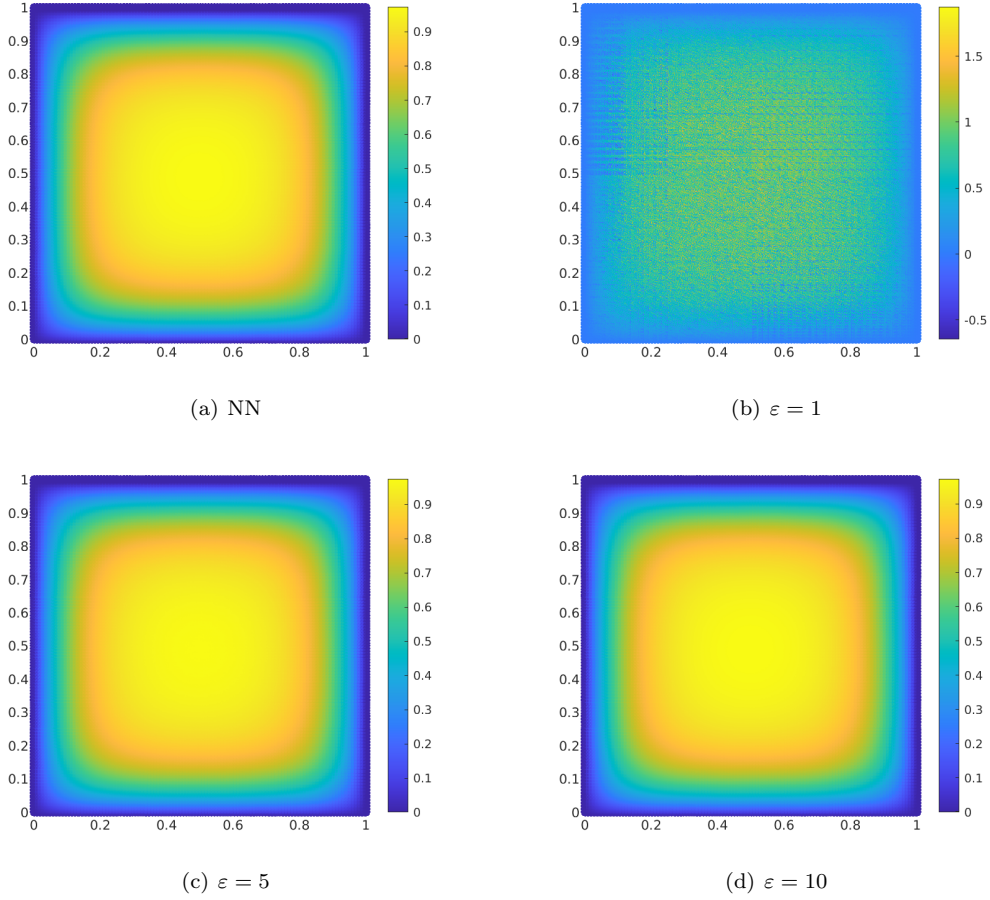


Figure 14: Numerical solution for the function f_4 using 640×640 evaluation points with IMQRBF.

4.2.2 Boundary value problem

We use the two dimensional linear elliptic boundary value problem

$$\begin{aligned} u_{xx} + u_{yy} &= -4\pi^2 \sin(2\pi xy)(x^2 + y^2), \quad (x, y) \in [0, 1] \times [0, 1], \\ u(x, y) &= \sin(2\pi xy), \quad (x, y) \in \partial([0, 1] \times [0, 1]) \end{aligned} \quad (26)$$

as a steady PDE test problem for the shape parameter strategies. The exact solution of the boundary value problem is $\sin(2\pi xy)$. We use collocated RBF-FD for this problem.

When considering the GARBF kernel, we again observe a greater sensitivity of the method with respect to the chosen ε , namely, that not only there is no fixed valued ε that performs better than the adaptive ε provided by the neural network, but also for poorly chosen ε ($\varepsilon = 1, 5, 10$), the approximation eventually blows-up, as shown in Table 10.

Table 10: The error using RBF-FD method using different strategies for Poisson equation with exact solution $\sin(2\pi xy)$ for structured grid with GARBF.

# interpolation/ evaluation points	NN	$\varepsilon = 1$	$\varepsilon = 5$	$\varepsilon = 10$	$\varepsilon = 100$
10×10	1.9403e-01	2.5470e-03	4.9695e-02	1.3311e-01	3.3161e-01
20×20	8.4645e-02	6.8800e-04	1.5314e-02	5.5160e-02	3.6776e-01
40×40	2.7915e-02	2.9304e-04	4.0221e-03	1.6304e-02	3.5368e-01
80×80	7.6639e-03	1.7146e-02	1.0174e-03	4.2514e-03	2.0177e-01
160×160	2.0625e-03	4.8929e-01	2.7545e-04	1.0735e-03	8.1534e-02
320×320	5.9784e-04	5.4754e+03	9.1389e-03	3.1306e-04	2.5303e-02
640×640	9.0457e-04	2.1826e+02	1.0231e+03	2.8746e-02	6.7143e-03

The error when using the IMQRBF kernel with constant shape parameters ($\varepsilon = 1, 5, 10, 100$) and variable shape parameter strategies are listed in Table 11. We see a clear advantage of the new method with respect to the constant shape parameter strategy. The errors blow-up in all the cases except when using the NN. The numerical solution obtained by using NN and constant shape parameters with 640×640 evaluation points is shown in the 15. We observe that the numerical solution is almost the same for NN and $\varepsilon = 10$.

Table 11: The error using RBF-FD method with different strategies for Poisson equation with exact solution $\sin(2\pi xy)$ on a structured grid with IMQRBF.

# interpolation/ evaluation points	NN	$\varepsilon = 1$	$\varepsilon = 5$	$\varepsilon = 10$	$\varepsilon = 100$
10×10	1.8630e-01	3.8201e-03	6.0522e-02	1.4643e-01	3.2945e-01
20×20	8.7444e-02	9.8806e-04	2.5272e-02	6.5721e-01	3.5997e-01
40×40	3.7178e-02	2.4926e-04	7.7340e-03	2.6150e-02	3.3186e-01
80×80	1.2454e-02	9.0683e-03	2.0447e-03	7.8927e-03	2.1501e-01
160×160	3.6264e-03	1.0339e-01	5.1784e-04	2.0813e-03	9.1097e-02
320×320	1.0744e-03	3.1287e+02	7.9589e-04	5.2789e-04	3.7253e-02
640×640	4.3698e-04	7.0244e-01	6.4113e-02	8.9551e-04	1.1979e-02

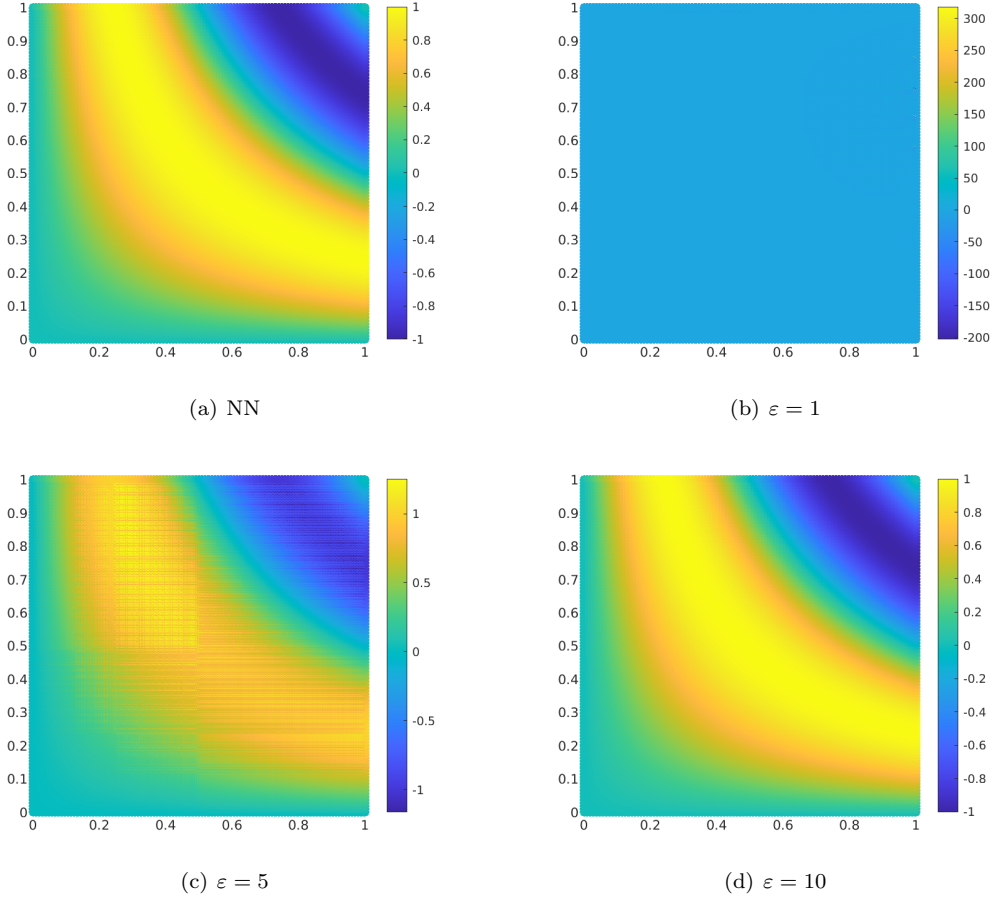


Figure 15: Numerical solution for the Poisson equation using 640×640 evaluation points with IMQRBF.

5 Discussion and conclusion remarks

We presented a methodology to train a neural network in an unsupervised fashion to predict a good shape parameter for given type of basis functions and size of stencil, taking as input location or relative distance of the interpolation nodes.

We studied different sizes of stencil $n = 5, 7, 10$ and found that $n = 10$ seems to lead to a better interpolation performance. This makes sense as we are using more interpolation points.

We also studied the different representation of the features. While coordinate-based features appeared more appealing and less costly for 2 and 3-dimension extensions, our numerical experiments demonstrate that using the relative distance between the interpolation points leads to a better performance (see Appendix A for a coordinate-based features approach in 1D). Furthermore, the distance-based features are naturally shift invariant and can be made rotation invariant in higher dimensions.

We considered two types of radial basis kernels (IMQRBF and GARBF) plus a constant basis function. This methodology can be extended to different basis kernels without much effort, except retraining the network.

Still on the two considered radial basis kernels for constant shape parameter strategy, the performance of GARBF is similar to the one of IMQRBF, but in most of the simulations the results with IMQRBF are more robust since the blow-up happens later. In our experiments, we observe that the results for the neural network strategy with GARBF are much better than IMQRBF.

In general, we have observed a negligible overhead by using the proposed method in comparison to a fixed shape parameter ε . Furthermore, it is well known that RBF methods are, in general, very competitive when compared with traditional FDM/FEM [28, 29, 30].

The presented methodology is very flexible in terms of size of the stencil, basis functions, desired matrix condition number range (in our work we set it to be between 10^{10} and 10^{12}). The main challenges are the correct description of the input features and the dataset generation, for which we provide our methodology as well.

5.1 Future work

Overall, the different tasks used to test our neural network in 1D show that this methodology is robust across a large range of distributions in points, both when considering equidistant and non-equidistant points. In 2D, we presented a neural network that considers a simple grid-like distribution of points and estimates a suitable shape parameter ε .

Although we have shown that this proposed methodology is robust across different tasks, it requires a specific structure on the cloud points. In the future, we would like to consider generic clouds of points. This comes with a few difficulties, e.g.: if we consider the distance-based features, which seems like the more suitable choice due to easily guaranteeing shift and rotation invariance, it leads to a feature space of dimension $\binom{n}{2}$ for n nodes, as opposed to a feature space of dimension $2n$ when considering coordinate-based features. One possibility would be to consider graph neural networks which are more suited for graph-like data, as we can interpret the cloud of points as graphs [31].

Another issue is on how to best generate the training data. Ultimately, we are interested in integrating these methods with (local) RBF-FD type methods so there is often some structure in the stencil. In particular, it is important to have a good sampling of the interior of the domain, as well as at the boundaries. This means that we have to identify strategies to generate a dataset that has a good covering of the input space. We can achieve this through a more detailed sampling strategy, balancing the number of points at the boundary and in the interior.

Acknowledgments

We take this opportunity to thank Fabian Mönkeberg for very helpful discussions.

Fundings

FNM was supported by the Institute of Mathematics at the University of Zürich. MHV was supported by the Michigan Institute for Data Science research fellowship at the University of Michigan and the Department of Mathematics at the University of Michigan. PÖ was supported by the Gutenberg Research College, JGU Mainz.

References

- [1] Gregory E. Fasshauer. Meshfree approximation methods with MATLAB. *World Scientific*, 6, 2007.
- [2] Natasha Flyer, Grady B. Wright, and Bengt Fornberg. Radial basis function-generated finite differences: A mesh-free method for computational geosciences. *Handbook of geomathematics*, pages 1–30, 2014.
- [3] Holger Wendland. *Scattered Data Approximation*, volume 17. Cambridge University Press, 2004.
- [4] Damiana Lazzaro and Laura B. Montefusco. Radial basis functions for the multivariate interpolation of large scattered data sets. *J. Comput. Appl. Math.*, 140(1-2):521–536, 2002.
- [5] Bengt Fornberg and Natasha Flyer. Accuracy of radial basis function interpolation and derivative approximations on 1-D infinite grids. *Advances in Computational Mathematics*, 23(1-2):5–20, 2005.
- [6] Natasha Flyer, Bengt Fornberg, Victor Bayona, and Gregory A. Barnett. On the role of polynomials in RBF-FD approximations. I: Interpolation and accuracy. *J. Comput. Phys.*, 321:21–38, 2016.

- [7] Oleg Davydov and Dang Thi Oanh. On the optimal shape parameter for gaussian radial basis function finite difference approximation of the poisson equation. *Computers & Mathematics with Applications*, 62(5):2143–2161, 2011.
- [8] Bengt Fornberg and Grady Wright. Stable computation of multiquadric interpolants for all values of the shape parameter. *Computers & Mathematics with Applications*, 48(5-6):853–867, 2004.
- [9] Michael Mongillo. Choosing basis functions and shape parameters for radial basis function methods. *SIAM undergraduate research online*, 4(190-209):2–6, 2011.
- [10] Mojtaba Ranjbar. A new variable shape parameter strategy for gaussian radial basis function approximation methods. *Annals of the University of Craiova-Mathematics and Computer Science Series*, 42(2):260–272, 2015.
- [11] Rolland L. Hardy. Multiquadric equations of topography and other irregular surfaces. *Journal of Geophysical Research (1896-1977)*, 76(8):1905–1915, 1971.
- [12] Richard Franke. Scattered data interpolation: tests of some methods. *Mathematics of Computation*, 38:181–200, 1982.
- [13] Bengt Fornberg and Cécile Piret. On choosing a radial basis function and a shape parameter when solving a convective pde on a sphere. *Journal of Computational Physics*, 227(5):2758–2780, 2008.
- [14] Grady B. Wright and Bengt Fornberg. Stable computations with flat radial basis functions using vector-valued rational approximations. *Journal of Computational Physics*, 331:137–156, 2017.
- [15] John C. Mairhuber. On Haar’s theorem concerning Chebychev approximation problems having unique solutions. *Proc. Am. Math. Soc.*, 7:609–615, 1956.
- [16] Philip C. jun. Curtis. n -parameter families and best approximation. *Pac. J. Math.*, 9:1013–1027, 1959.
- [17] Jan Glaubitz, Jan Nordström, and Philipp Öffner. Energy-stable global radial basis function methods on summation-by-parts form. *arXiv preprint arXiv:2204.03291*, 2022.
- [18] Jan Glaubitz, Jan Nordström, and Philipp Öffner. Summation-by-parts operators for general function spaces. *accepted in SIAM Journal on Numerical Analysis*, 2022.
- [19] Andrei I. Tolstykh and D. A. Shirobokov. On using radial basis functions in a “finite difference mode” with applications to elasticity problems. *Computational Mechanics*, 33(1):68–79, 2003.
- [20] Pankaj K. Mishra, Gregory E. Fasshauer, Mrinal K. Sen, and Leevan Ling. A stabilized radial basis-finite difference (RBF-FD) method with hybrid kernels. *Computers & Mathematics with Applications*, 77(9):2354–2368, 2019.
- [21] Suranon Yensiri and Ruth J. Skulku. An investigation of radial basis function-finite difference (rbf-fd) method for numerical solution of elliptic partial differential equations. *Mathematics*, 5(4):54, 2017.
- [22] Steven J. Nowlan and Geoffrey E. Hinton. Simplifying neural networks by soft weight-sharing. *Neural Comput.*, 4:473–493, 1992.
- [23] Rolland L. Hardy. Multiquadric equations of topography and other irregular surfaces. *Journal of geophysical research*, 76(8):1905–1915, 1971.
- [24] Richard Franke. Scattered data interpolation: tests of some methods. *Mathematics of computation*, 38(157):181–200, 1982.
- [25] Gregory E. Fasshauer. Newton iteration with multiquadrics for the solution of nonlinear pdes. *Computers & Mathematics with Applications*, 43(3-5):423–438, 2002.

- [26] Gregory E. Fasshauer, Eugene C. Gartland, and Joseph W. Jerome. Newton iteration for partial differential equations and the approximation of the identity. *Numerical Algorithms*, 25(1):181–195, 2000.
- [27] Malgorzata A. Jankowska, Andreas Karageorghis, and Ching-Shyang Chen. Improved kansa rbf method for the solution of nonlinear boundary value problems. *Engineering Analysis with Boundary Elements*, 87:173–183, 2018.
- [28] Jichun Li, Alexander H.-D. Cheng, and Ching-Shyang Chen. A comparison of efficiency and error convergence of multiquadric collocation method and finite element method. *Eng. Anal. Bound. Elem.*, 27(3):251–257, 2003.
- [29] Ali Safdari-Vaighani, Alfa Heryudono, and Elisabeth Larsson. A radial basis function partition of unity collocation method for convection-diffusion equations arising in financial applications. *J. Sci. Comput.*, 64(2):341–367, 2015.
- [30] E. Larsson and B. Fornberg. A numerical study of some radial basis function based solution methods for elliptic PDEs. *Comput. Math. Appl.*, 46(5-6):891–902, 2003.
- [31] Jie Zhou, Ganqu Cui, Shengding Hu, Zhengyan Zhang, Cheng Yang, Zhiyuan Liu, Lifeng Wang, Changcheng Li, and Maosong Sun. Graph neural networks: A review of methods and applications. *AI Open*, 1:57–81, 2020.

A Results for coordinate-based features in one dimensional case

A.1 One-dimensional interpolation

Fig. 16 shows the convergence plot for the function f_1 with IMQRBF using shape parameters obtained by the neural network strategy based on coordinate-based features and the constant shape parameters as a function of the number of centers for equidistant and non-equidistant points. Fig. 17 shows the convergence plot for the function f_2 with IMQRBF using shape parameters obtained by the neural network strategy based on coordinate-based features and the constant shape parameters as a function of the number of centers for equidistant and non-equidistant points. The results for these two test cases are qualitatively similar to the ones obtained using distance-based features.

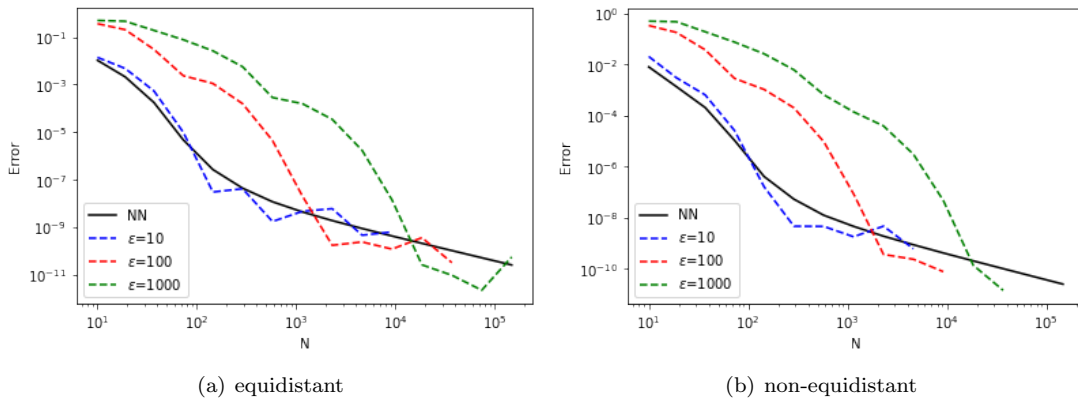


Figure 16: Convergence plot for the function f_1 using a neural network strategy and constant shape parameters in 1D with IMQRBF.

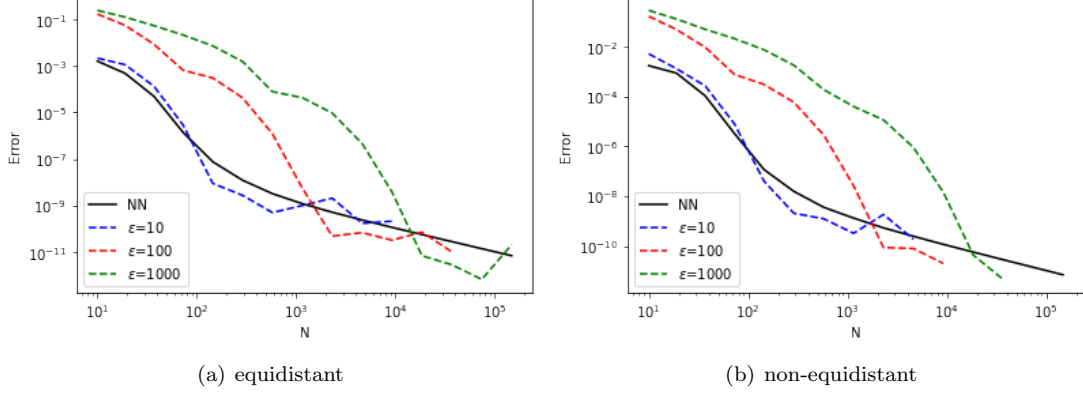


Figure 17: Convergence plot for the function f_2 using a neural network strategy and constant shape parameters in 1D with IMQRBF.

A.2 One-dimensional time-dependent problem

We compare the RBF-FD method with the shape parameters obtained by the neural network strategy based on coordinate-based features with a FDM, a FEM and a RBF-FD method with constant shape parameters. In Table 12 and Table 13, the errors are listed for the heat equation (21) with the initial condition (22) for equidistant and non-equidistant points, respectively. In Table 14 and Table 15, the errors are listed for the heat equation (21) with the initial condition (24) for equidistant and non-equidistant points, respectively. We can observe that we have the same results as for distance-based features for equidistant points, but the results for non-equidistant points is better for distance-based features.

Table 12: The error using different schemes for equidistant points with initial condition $-x^2 + x$ with IMQRBF.

N	FDM	FEM	NN	$\varepsilon = 1$	$\varepsilon = 10$	$\varepsilon = 100$
N=10	1.5283e-04	1.5152e-04	1.9181e-03	6.9435e-06	5.9731e-03	1.4708e-02
N=19	4.1141e-05	3.9723e-05	3.2476e-04	8.6638e-07	6.0268e-04	1.5342e-02
N=37	1.1152e-05	9.8825e-06	1.5181e-05	-	4.4987e-05	1.4919e-02
N=73	3.3997e-06	2.4375e-06	1.9688e-06	-	2.9077e-06	1.0560e-02
N=145	1.4322e-06	9.6827e-07	1.2384e-06	-	9.0652e-07	1.1204e-03

Table 13: The error using different schemes for non-equidistant points with initial condition $-x^2 + x$ with IMQRBF.

N	FDM	FEM	NN	$\varepsilon = 1$	$\varepsilon = 10$	$\varepsilon = 100$
N=10	3.0018e-03	3.1917e-03	5.4642e-03	2.9977e-03	9.5229e-03	1.4744e-02
N=19	3.1257e-03	3.1769e-03	3.3695e-03	3.1253e-03	4.0648e-03	1.5521e-02
N=37	3.2019e-03	3.2151e-03	3.3639e-03	-	3.7745e-03	1.5813e-02
N=73	3.2435e-03	3.2469e-03	3.2547e-03	-	3.2918e-03	1.4598e-02
N=145	3.2653e-03	3.2662e-03	3.2656e-03	-	3.2652e-03	8.4020e-03

Table 14: The error using different schemes for equidistant points with initial condition $6 \sin(\pi x)$ with IMQRBF.

N	FDM	FEM	NN	$\varepsilon = 1$	$\varepsilon = 10$	$\varepsilon = 100$
N=10	3.5303e-03	3.4600e-03	4.4323e-02	6.2511e-05	1.3867e-01	3.4160e-01
N=19	9.4294e-04	9.1108e-04	7.4256e-03	1.7241e-05	1.3833e-02	3.5640e-01
N=37	2.5361e-04	2.2566e-04	3.5209e-04	-	1.0468e-03	3.4678e-01
N=73	7.5759e-05	5.4121e-05	4.3776e-05	-	6.5944e-05	2.4553e-01
N=145	3.0626e-05	2.0276e-05	2.6383e-05	-	1.8624e-05	2.6311e-02

Table 15: The error using different schemes for non-equidistant points with initial condition $6 \sin(\pi x)$ with IMQRBF.

N	FDM	FEM	NN	$\varepsilon = 1$	$\varepsilon = 10$	$\varepsilon = 100$
N=10	6.9932e-02	7.4578e-02	1.2766e-01	6.9815e-02	2.2221e-01	3.4248e-01
N=19	7.2790e-02	7.4039e-02	7.8271e-02	7.2770e-02	9.4567e-02	3.6052e-01
N=37	7.4552e-02	7.4875e-02	7.8321e-02	-	8.7929e-02	3.6743e-01
N=73	7.5520e-02	7.5602e-02	7.5785e-02	-	7.6662e-02	3.4017e-01
N=145	7.6028e-02	7.6048e-02	7.6035e-02	-	7.6025e-02	1.9665e-01

B Results for 1D GARBF

B.1 Interpolation

Fig. 18 shows the convergence plot for the function f_1 with GARBF using shape parameters obtained by the neural network strategy and the constant shape parameters as a function of centers for equidistant and non-equidistant points. Fig. 19 shows the convergence plot for the function f_2 with GARBF using shape parameters obtained by the neural network strategy and the constant shape parameters as a function of the number of centers for equidistant and non-equidistant points.

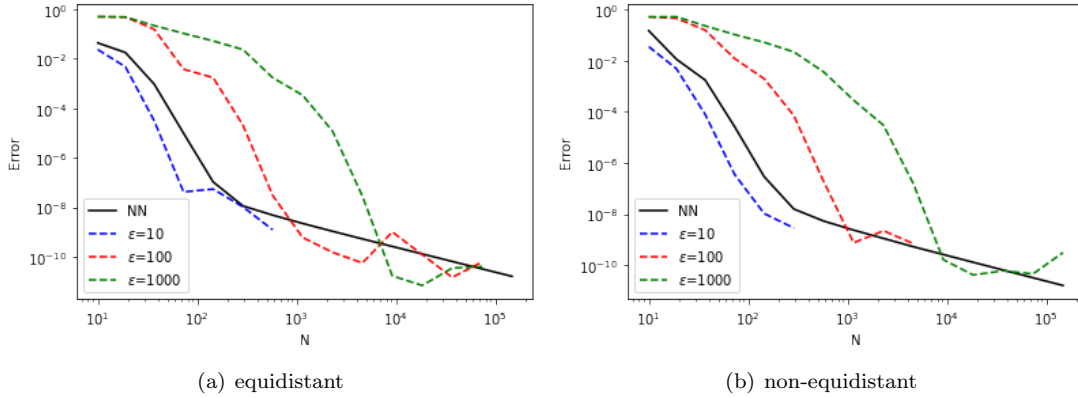


Figure 18: Convergence plot for the function f_1 using a neural network strategy and constant shape parameters in 1D with GARBF.

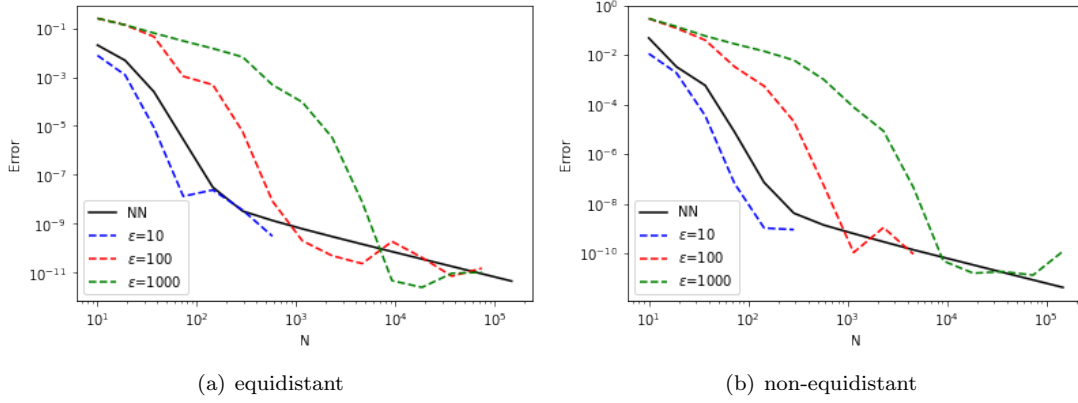


Figure 19: Convergence plot for the function f_2 using a neural network strategy and constant shape parameters in 1D with GARBF.

B.2 Time-dependent PDE

In this section we will focus on (21), with two different initial and boundary conditions using GARBFs. We consider the initial condition (22) and boundary condition (23). And, the same problem with initial condition (24) and boundary condition (25).

Table 16: The error using different schemes for equidistant points with initial condition $-x^2 + x$ with GARBF.

N	FDM	FEM	NN	$\varepsilon = 1$	$\varepsilon = 10$	$\varepsilon = 100$
N=10	1.5283e-04	1.5152e-04	1.1940e-02	1.2809e-06	3.7287e-03	1.4734e-02
N=19	4.1141e-05	3.9723e-05	1.7786e-03	-	7.5650e-04	1.5486e-02
N=37	1.1152e-05	9.8825e-06	1.0877e-04	-	5.8281e-06	1.5440e-02
N=73	3.3997e-06	2.4375e-06	2.0636e-06	-	8.7901e-07	1.0878e-02
N=145	1.4322e-06	9.6827e-07	9.5398e-07	-	-	5.2185e-03

Table 17: The error using different schemes for non-equidistant points with initial condition $-x^2 + x$ with GARBF.

N	FDM	FEM	NN	$\varepsilon = 1$	$\varepsilon = 10$	$\varepsilon = 100$
N=10	3.0018e-03	3.1917e-03	1.3410e-02	2.9978e-03	1.0159e-02	1.4763e-02
N=19	3.1257e-03	3.1769e-03	6.5013e-03	3.2367e-03	4.0193e-03	1.5594e-02
N=37	3.2019e-03	3.2151e-03	4.4667e-03	-	3.2074e-03	1.6058e-02
N=73	3.2435e-03	3.2469e-03	3.2711e-03	-	3.2434e-03	1.5441e-02
N=145	3.2653e-03	3.2662e-03	3.2653e-03	-	-	1.1978e-02

Table 18: The error using different schemes for equidistant points with initial condition $6 \sin(\pi x)$ with GARBF.

N	FDM	FEM	NN	$\varepsilon = 1$	$\varepsilon = 10$	$\varepsilon = 100$
N=10	3.5303e-03	3.4600e-03	2.7771e-01	1.6327e-05	8.6403e-02	3.4220e-01
N=19	9.4294e-04	9.1108e-04	4.1225e-02	-	1.7501e-02	3.5974e-01
N=37	2.5361e-04	2.2566e-04	2.5212e-03	-	1.3377e-04	3.5886e-01
N=73	7.5759e-05	5.4121e-05	4.6727e-05	-	1.8014e-05	2.5313e-01
N=145	3.0626e-05	2.0276e-05	1.9743e-05	-	-	1.2224e-01

Table 19: The error using different schemes for non-equidistant points with initial condition $6 \sin(\pi x)$ with GARBF.

N	FDM	FEM	NN	$\varepsilon = 1$	$\varepsilon = 10$	$\varepsilon = 100$
N=10	6.9932e-02	7.4578e-02	3.1237e-01	6.9816e-02	2.3717e-01	3.4291e-01
N=19	7.2790e-02	7.4039e-02	1.5131e-01	7.2774e-02	9.3198e-02	3.6222e-01
N=37	7.4552e-02	7.4875e-02	1.0438e-01	-	7.4683e-02	3.7301e-01
N=73	7.5520e-02	7.5602e-02	7.6176e-02	-	7.5516e-02	3.5991e-01
N=145	7.6028e-02	7.6048e-02	7.6028e-02	-	-	2.8037e-01